CrossMark

Three-dimensional scaffolding framework of porous carbon nanosheets derived from plant wastes for high-performance supercapacitors

Chong Chen [a,c], Dengfeng Yu [b], Gongyuan Zhao [a], Baosheng Du [b], Wei Tang [b], Lei Sun [a],
Ye Sun [b,**], Flemming Besenbacher [c,***], Miao Yu [a,*]

[a] State Key Laboratory of Urban Water Resource and Environment, School of Chemical Engineering and Technology, Harbin Institute of Technology, Harbin 150001, China
[b] Condensed Matter Science and Technology Institute, Harbin Institute of Technology, Harbin 150001, China
[c] Interdisciplinary Nanoscience Center (iNANO) and Department of Physics and Astronomy, Aarhus University, Aarhus 8000, Denmark

ARTICLE INFO

ABSTRACT

Utilizing carbon materials derived from sustainable biomass on supercapacitors has become particularly attractive recently. High-performance activated carbons (ACs) based on inexpensive, abundant but unwanted natural wastes are highly preferred. In this work, using dry elm samara as the prototype, we demonstrate that three-dimensional (3-D) scaffolding frameworks of highly porous carbon nanosheets (PCNSs) can be derived from plant wastes having specific natural morphology, *i.e.* half-transparent thin flakes, through a facile carbonization and activation treatment. The products possess a high accessible surface area induced by the 3-D framework, and a high density of micro-pores, which benefit large ion storage and high-rate ion transfer. In addition to the electric double-layer capacitor, the heteroatom doping evokes the faradic contribution. PCNS activated by 6 mol L^{-1} KOH (PCNS-6) exhibited a rather high specific capacitance of 470 F g^{-1} and 310 F g^{-1} at a current density of 1.0 A g^{-1} respectively in a three- and two-electrode system using 6 mol L^{-1} KOH electrolyte, among the highest ever reported for carbon materials derived from biomass. Furthermore, the high rate capability (72% and 64% capacitance retention at 200 mV s^{-1} and 20 A g^{-1}, respectively) as well as the high cycling stability (2% loss over 50,000 cycles) significantly potentiate the supercapacitor properties of the product. Additionally, an energy density as high as 25.4 Wh kg^{-1} at the power density of 15 kW kg^{-1} was verified in 1-ethyl-3-methylimidazolium tetrafluoroborate (EMIMBF$_4$) electrolyte. Most importantly, it is demonstrated that 3-D scaffolding PCNS frameworks can be easily achieved from different plant wastes sharing common features. This work provides a clear strategy on how to select promising plant-waste candidates for high-performance ACs applied on energy storage.

© 2016 Elsevier Ltd. All rights reserved.

1. Introduction

The global grand challenges faced by society today due to the scarcity of fossil fuels and the severe environmental issues, together with the simultaneous demands from economic development, have stimulated tremendous interest in high-performance energy storage devices [1]. In particular, as the complement or replacement of batteries, supercapacitors based on activated carbons (ACs) have become considerably appealing and prosperous

due to the rapid charging rate, long cycling life and large discharge capacity [1,2]. However, the low energy density and poor electrical conductivity of commercially available supercapacitors have largely limited their application prospects [3], and have actuated considerable interest in exploring new ACs with advanced properties.

The actual energy stored in the supercapacitor is proportional to its capacitance and the square of operating voltage of electrolytes. Both are mainly determined by the specific surface area (SSA), pore structure and heteroatom doping effects of the electrode materials. Although the absolute SSA measured by the Brunauer-Emmett-Teller (BET) method has been usually reported in the literature as a key parameter to evaluate the ACs' properties, it is actually not meaningful without an appropriate structure to enable a full or high utilization of the SSA. There are two major

* Corresponding author.
** Corresponding author.
*** Corresponding author.
E-mail addresses: sunye@hit.edu.cn (Y. Sun), fbe@inano.au.dk (F. Besenbacher), miaoyu_che@hit.edu.cn (M. Yu).

strategies to achieve a high accessible surface area. One is to construct hierarchical porous structures combining micro-, meso- and macro-pores, the other is to design three-dimensional (3-D) scaffolding frameworks of porous carbons which avoid over-lapping-induced SSA loss and favor ion diffusion by providing short pathways. Substantial effort has been devoted to the fabri-cation of the two kinds of ACs, but normally with the use of complicated and expensive synthesis as well as irritant or corro-sive substances [3–10].

In addition to the high performance of products, the cost, sustainability, environmental friendliness, universality of the re-sources, and simpleness of fabrication are all essential concerns for large-scale production. Very recently, utilizing carbon materials derived from sustainable biomass for energy storage has become particularly fascinating [11,12]. It has been demonstrated by many successful examples that ACs with good capacitive performance can be obtained from biosources, *e.g.* lotus pollen [13], silk [14], protein [15], soya bean [16], hemp [17], yogurt [18], eggshell membrane [19], human hair [20], *etc.* although some of them are apparently luxury, rare, or difficult to collect. It would be more ideal if high-performance ACs can be produced from inexpensive, abundant but unwanted natural wastes. More importantly, all previous reports only addressed individual cases of single biomass without any explicit principle to follow. It is, therefore, paramount to explore the common features and underlying rules for the se-lection of promising raw materials.

In this work, using dry elm samara (DES) as the prototype, we demonstrate that 3-D scaffolding frameworks of highly porous carbon nanosheets (PCNSs) can be derived from plant wastes having the specific natural morphology, *i.e.* half-transparent thin flakes, through a simple carbonization and activation treatment (Scheme 1). Due to the large accessible surface area of the 3-D framework, the high density of micro-pores and the heteroatom doping, the PCNSs activated by 6 mol L^{-1} KOH (PCNS-6) exhibited a rather high charge storage capacity with a specific capacitance of 470 F g^{-1} and 310 F g^{-1} at a current density of 1.0 A g^{-1} respec-tively in a three- and two-electrode system using 6 mol L^{-1} KOH electrolyte, among the highest ever reported for carbon materials derived from biomass. Furthermore, the high rate capability (72% and 64% capacitance retention at 200 mV s^{-1} and 20 A g^{-1}, re-spectively) as well as the high cycling stability (2% loss over 50,000 cycles) significantly potentiate the supercapacitor properties of the product. Additionally, an energy density as high as 25.4 Wh kg^{-1} at the power density of 15 kW kg^{-1} was verified in 1-ethyl-3-methylimidazolium tetrafluoroborate (EMIMBF$_4$) electrolyte. The

high performance on energy storage was directly demonstrated by lighting aligned LED bulbs and powering a small electric fan, using a supercapacitor model with PCNS-6 as the electrode materials. Most importantly, by exploring a big variety of plant wastes, it is revealed that 3-D scaffolding PCNS frameworks can be easily achieved from those sharing the above-mentioned common fea-tures. This work may provide a clear strategy on how to select promising plant-waste candidates from innumerable biomass for ACs on high-performance supercapacitors.

2. Experimental section

2.1. Fabrication of the PCNS

DEM collected were thoroughly washed in water and then dried at 70 °C in a lab oven. Typically, DEM (5.0 g) were mixed with 50.0 ml of potassium hydroxide (KOH, Guoyao Chemical Re-agents Co., Ltd.) aqueous solution for 12 h. After removed extra aqueous solution by a simple filtration process, the KOH-treated elm samaras were dried in a vacuum oven at 100 °C for 10 h. The KOH/elm samaras mixture with a mass ratio of 1:1 was carbonized in argon at 700 °C for 2 h using a tube furnace. The as-grown samples were then treated with HCl solution (10 wt%), washed with deionized water, and dried at 100 °C for 12 h. The final pro-ducts are denoted as 'PCNS-*n*', where n (2, 4, 6, 8) indicates the concentration (*n*mol L^{-1}) of the KOH aqueous solution. DEM car-bonized at 700 °C for 2 h without KOH-treatment was used as the control group ('Control').

2.2. Instruments

The samples were characterized by field-emission scanning electron microscopy (FESEM, FEI, Quanta 200F), transmission electron microscopy (TEM, FEI, Tecnai-G2-F30), atomic force mi-croscopy (AFM, Bruker, MultiMode-8), X-ray diffraction (XRD, PANalytical, X'Pert Pro, with Cu Ka radiation), Raman spectroscopy (Renishaw with an excitation at 532 nm), and X-ray photoelectron spectroscopy (XPS, ESCALAB, 250Xi). SSA and pore size distribu-tion were measured by nitrogen adsorption-desorption isotherms at 77.4 K (Quantachrome Autosorb-iQ) after vacuum drying at 200 °C for 30 h. The SSA of the samples was calculated by a multi-point BET method. And the isotherms were further calculated by using a slit/cylindrical non-local density functional theory (DFT) model to deduce pore size distribution and total pore volume.

Scheme 1. Schematic illustration of PCNS derived from dry elm samaras.

2.3. Electrochemical measurement

Carbon sample (80 wt%), acetylene black (15 wt%) and poly-tetrafluoroethylene (PTFE) binder (5 wt%) were mixed in ethanol, then coated onto nickel-foam current collectors (1×1 cm^2), and dried at 120 °C for 12 h. The mass loading of the active materials in each working electrode was ~ 3 mg cm^{-2}. For the three-electrode system, Pt foil and Hg/HgO electrode were used as the counter and reference electrodes, respectively. The electrochemical performance was tested in 6 mol L^{-1} KOH electrolyte. For the two-electrode system (2032 stainless steel coin cell), both aqueous 6 mol L^{-1} KOH and EMIMBF$_4$ were used as the electrolyte, respectively. The dried electrodes (~ 3.0 mg cm^{-2}, 0.3 mm in thickness) were symmetrically assembled with glassy paper as the separator in a glove box filled with argon. The cyclic voltammetry (CV), galvanostatic charge-discharge, and electrochemical impedance spectroscopy (EIS) measurements were carried out using an electrochemical workstation (CHI660E, ChenHua Instruments Co. Ltd., Shanghai).

For the three-electrode system, the specific capacitance, specific energy density and specific power density derived from galvanostatic tests can be calculated by the following equations:

$$C = \frac{I\Delta t}{m\Delta V} \tag{1}$$

$$\rho = \frac{1}{V_{total} + 1/\rho_{carbon}} \tag{2}$$

$$C_v = C_g \rho \tag{3}$$

where C (F g^{-1}) is the specific capacitance; I (A) is the discharge current; Δt (s) is the discharge time; ΔV (V) is the potential window; m (mg) is the mass of the active materials; ρ (g cm^{-3}) is the density of electrode materials; V_{total} (cm^3 g^{-1}) is the total pore volume of active material measured by nitrogen isotherm; ρ_{carbon} is the density of carbon (2 g cm^{-3}); and C_v (F cm^{-3}) is the volumetric capacitance.

For the two-electrode system, the specific capacitances derived from galvanostatic tests can be calculated from the equations:

$$C = \frac{4I\Delta t}{m\Delta V} \tag{4}$$

$$C = \frac{2}{mv(V_b - V_a)} \int_{V_a}^{V_b} IdV \tag{5}$$

$$E = \frac{1}{8}C\Delta V^2 \tag{6}$$

$$P = \frac{E}{\Delta t} \tag{7}$$

where C (F g^{-1}) is the specific capacitance; v (V s^{-1}) is the scan rate; I (A) is the discharge current; V_b and V_a (V) are the high and low potential limit of the CV tests; E (Wh kg^{-1}) is the average energy density; P (W kg^{-1}) is the average power density; I (A) is the discharge current; Δt (s) is the discharge time; ΔV (V) is the potential window; and m (mg) is the total mass of the active materials.

## 3. Results and discussion

3.1. Characterization of the PCNS

Elm is a kind of common arbor widely spread throughout the northern hemisphere, especially in Northeast Asia. Fresh elm samaras are light-green oval flakes heaping up in branches in spring, and become pale-yellow and dry as plant wastes on the ground in summer. It is known that around 85.0 g of water, 8.5 g of carbohydrates, 3.8 g of protein, 1.0 g of fat, and 1.3 g of dietary fiber are contained in every 100.0 g of fresh elm samaras [21]. The DES were thoroughly washed in water, and then dehydrated at 70 °C in a lab oven. As revealed by the SEM results in Fig. 1, each DES has a special subtle sandwich structure composed of two layers of thin flakes and porous tubes strutted in between.

The morphology of all samples was characterized by both SEM and TEM. As depicted in Fig. 2a–b, after the direct pyrolysis, the flake-tube-flake sandwich configuration was disassembled into individual porous tubes and fragmental flakes. Excitingly, carbonization of the KOH-treated DES leaded to a completely new appearance, i.e. a 3-D scaffolding framework assembled and strutted by gauze-like nanosheets (Fig. 2c–f). Compared with the flake of Control group, these nanosheets were much thinner. The thickness was significantly decreased with the KOH concentration applied. At a KOH concentration ≥ 8 mol L^{-1}, the nanosheets were too thin to hold the 3-D frameworks with partial sections collapsed. The AFM results (Fig. S1) reveal that the thickness of the PCNS-6 was down to 1–2 nm.

The fine structure of the PCNS-6 was further explored by high-resolution TEM (refer to Fig. 2h), evidently revealing a high density of micropores on the nanosheets by the varied contrast. The porosity was then investigated via BET analysis of nitrogen adsorption-desorption isotherms (Fig. 3). As summarized in Table 1, the SSA of the products can be efficiently increased by the KOH treatment, and the porosity characteristics were strongly dependent on the KOH concentration. When the KOH concentration was increased from 4 to 6 mol L^{-1}, the SSA and pore volume were enlarged from 1424 to 1947 m^2 g^{-1} and 1.18–1.33 cm^3 g^{-1}, respectively. Both the PCNS-4 and PCNS-6 samples showed Type I+IV isotherms, where the sharp adsorption at low relative pressure (0–0.1) is indicative of microporosity, and the adsorption at higher relative pressure is corresponding to the presence of mesoporosity. As seen in Fig. 3f, calculated using DFT method, four sharp peaks were found in the pore size distribution plot of the PCNS-6, centered at 0.52, 0.82, 1.14 and 2.19 nm, respectively. It is worthy of noting that, besides the high SSA and the high density of micropores, the inherent 3-D strutted configuration of the PCNS samples may guarantee a high accessibility and utilization of the surface for ion storage. Moreover, enabled by the 3-D framework, the direct exposure of the highly porous nanosheets to the electrolyte may efficiently shorten the pathway and lower the resistance for ion diffusion. The distinct structural characteristics may endow the PCNSs considerable potentials on high-performance supercapacitors.

The products were then analyzed by XRD (Fig. 4a). The pattern of the Control sample showed a broad peak at $\sim 24°$, assigned to the carbon turbostratic stacking. In contrast, for the PCNS-4 and PCNS-6 samples, the peak at $\sim 24°$ became a shoulder while a large increase in the low-angle scatter was observed instead, indicating a high density of micropores. This further supports the TEM and adsorption-desorption isotherm results mentioned above. The chemical structure was characterized by Raman spectra. In Fig. 4b, the peak located at 1338 cm^{-1} (D-band) is attributed to the disorder induced by structural defects and impurities, and the one at 1586 cm^{-1} (G-band) is assigned to the stretching bond of sp^2 hybridized carbon [22,23]. For all given samples, the higher intensity
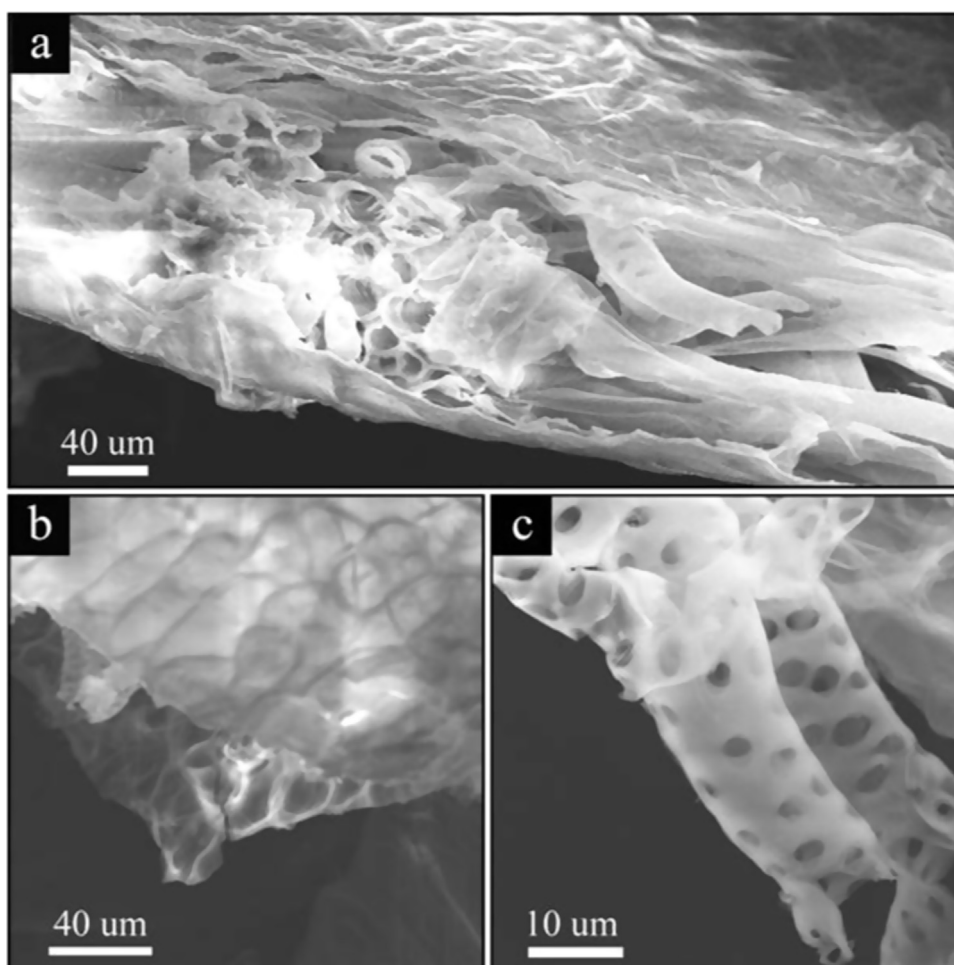
Fig. 1. (a) Side-view and (b) top-view SEM images of a cracked DES, showing a sandwich configuration composed of flakes and porous tube-like veins in between. (c) Zoomed-in SEM image of the porous tubes.

of G-band than that of the D-band indicates their partial graphitization, which benefits the conductivity hence the capacitance of the products. It is noted that the integrated intensity ratio (I_G/I_D) of the PCNS-4 (0.92) and PCNS-6 (0.93) samples were higher than that of the Control (0.88), likely due to a reduced amount of heterotoms in the products upon KOH treatment, as revealed by the XPS results below.

From the XPS survey of the Control (Fig. 5a), it is clear that three elements including carbon, oxygen and nitrogen were contained. As comparison, the nitrogen content of the PCNS-4 and PCNS-6 samples (Fig. 5b–c) was largely decreased to be 0.8% and 0.7% due to the KOH activation, while the percentage of oxygen was also reduced from 13.0% in the Control to 5.2% in the PCNS-4% and 4.9% in the PCNS-6. Each C1s spectrum (Fig. 5d–f) can be deconvoluted into five peaks centered at 284.6, 285.1, 285.6, 286.6 and 288.4 eV, assigned to C=C, C–C, C–N, C–O and C=O bond [24–26], respectively. Consistent with the XRD results, the relative intensity of C=C peak corresponding to sp^2 hybridized graphitic carbon was decreased upon the KOH treatment, supporting the formation of high density of micropores in the products. The high-resolution O1s spectrum (Fig. 5g–i) can be deconvoluted into two peaks located at 532.2 and 533.5 eV, corresponding to C=O and O–C=O groups [27]. The largely reduced relative intensity of the former peak indicates a reduction in carboxyl ingredients following KOH treatment. The N1s spectrum of the Control sample (Fig. 5j) can be deconvoluted into two peaks centered at 398.0 and 400.8 eV, corresponding to pyridinic nitrogen (N-6) and

quaternary nitrogen (N-4), respectively. Interestingly, for the PCNS samples (Fig. 5k–l), besides N-4, we observed another peak at 400.1 eV corresponding to pyrrolic nitrogen (N-5), which is known as a major nitrogen configuration contributing to pseudocapacitance [28]. As demonstrated in the literature, the dosing of oxygen and nitrogen heteroatoms can effectively improve the pseudocapacitance and wettability of carbon electrode materials [29].

3.2. Electrochemical properties in a three-electrode system

The performance of the PNCS-4, PNCS-6 and Control samples as supercapacitor electrodes was firstly investigated in a three-electrode system using 6 mol L^{-1} KOH as the electrolyte at room temperature. The CV curves collected at 20 mV s^{-1} and galvanostatic charge-discharge results at 2 A g^{-1} are presented in Fig. 6a–b. Apparently, compared with the Control sample, all PNCS products showed largely improved electrochemical properties. The PNCS-6 exhibited a better capacitance performance than the PNCS-4. We then focused on the PNCS-6. In Fig. 6a, the rectangular voltammetry curve in a voltage window from − 1.0 to 0 V scanned at 20 mV s^{-1} indicates the dominance and good performance of the electrical double-layer capacitors (EDLC) formed at the electrode-electrolyte interface during the charge-discharge process. The CV curves at a scan rate ranging from 5 to 100 mV s^{-1} are presented in Fig. S2a. The rectangular shape maintained at a high scan rate of 100 mV s^{-1} reveals the quick charge transfer of the EDLC, nicely supporting our anticipation on the special configuration of 3-D scaffolding PNCS framework. Meanwhile, the
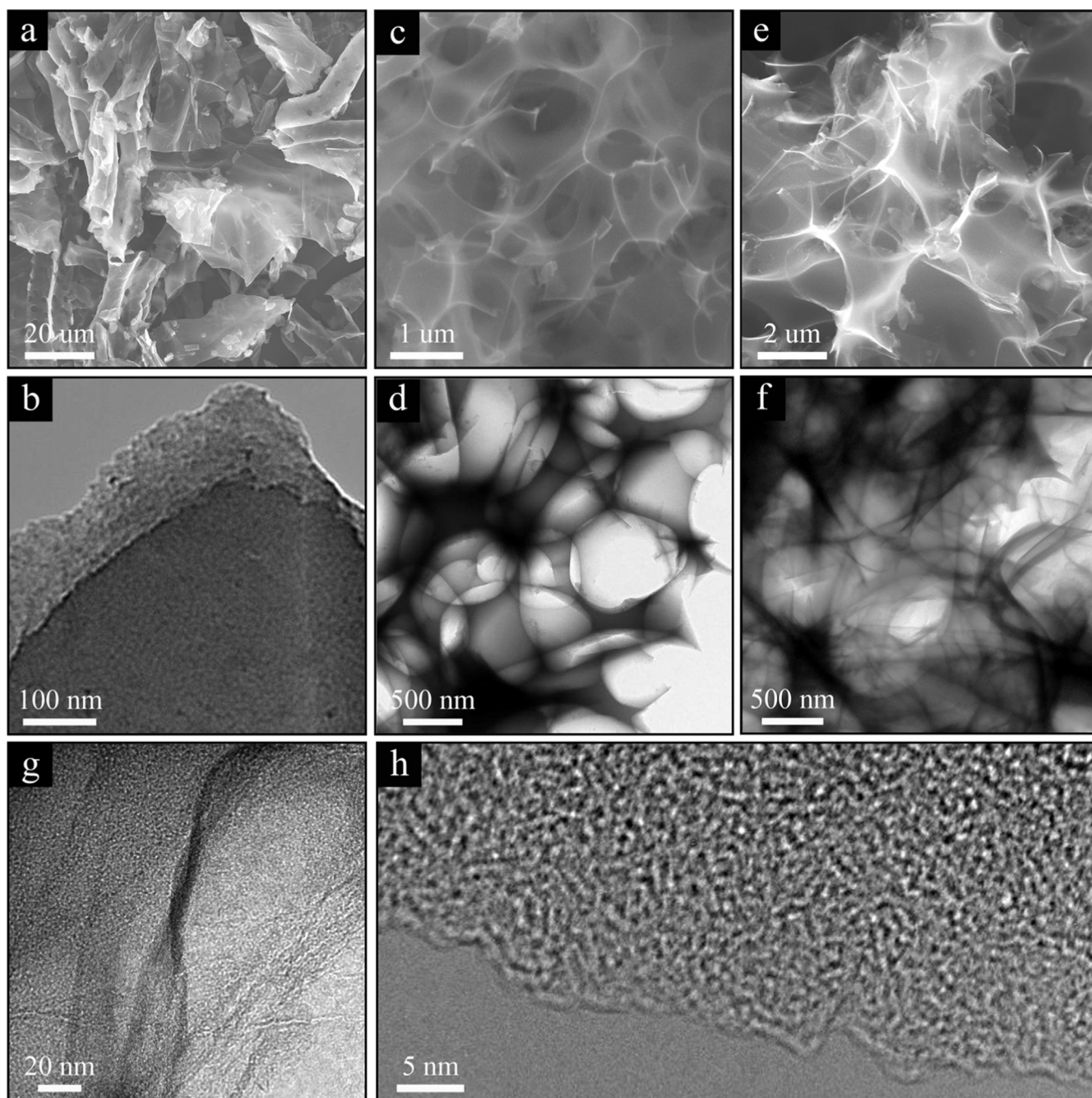
Fig. 2. SEM and TEM images of (a–b) the Control, (c–d) the PCNS-4, and (e–f) the PCNS-6 samples. (g–h) High-resolution TEM images of the PCNS-6, revealing the high density of micropores on the ultrathin sheet.

deviations from triangular shapes of the galvanostatic charge-discharge curve indicate the contribution of pseudocapacitance because of the effect of doped heteroatoms (Fig. S2b).

The gravimetric capacitance and volumetric capacitance of the Control, PCNS-4, PCNS-6 samples were calculated at various current densities ranging from 1 to 20 A g^{-1} (Fig. 6c–d), resulting in a value as high as 470 F g^{-1} and 257 F cm^{-3}, respectively, at a current density of 1.0 A g^{-1}. It is worth emphasizing that the value of 470 F g^{-1} is much higher than that of most of reported carbon electrode materials derived from biomass (Table 2), although most of them were apparently given at a much lower current density than what we used here. Due to the limited time allowing for electrolyte ions diffusion, the specific capacitance normally suffers a large reduction at higher current densities, as reported in the literature [20,22,30]. But in our case, rather high specific capacitance of the PCNS-6 can be still obtained at a

much higher current density, e.g. 300 F g^{-1} at 10 A g^{-1}. And even at a current density as high as 20 A g^{-1}, a specific capacitance of 266 F g^{-1} was still preserved, further confirming the high-rate ion transfer for the PCNS-6.

Comparing the data reported in the literature (Table 2), it is obvious that a high SSA value does not necessarily induce a high capacitance. For instance, while the low SSA (only 221.2 $m^2\,g^{-1}$) of the ACs derived from eggshell membrane give a high capacitance of 297 F g^{-1} [19], the much higher SSA (2557.3 $m^2\,g^{-1}$, more than 11 times as that of the former) of the carbon-based nanoplates fabricated from regenerated silk fibroin showed a lower capacitance of 264 F g^{-1} [14]. The large deviations can be mainly attributed to the difference between their accessible surface areas, which can be largely benefited by a 3-D scaffolding structure, such as the case in Ref. [19]. Therefore, an appropriate structure which enables a high
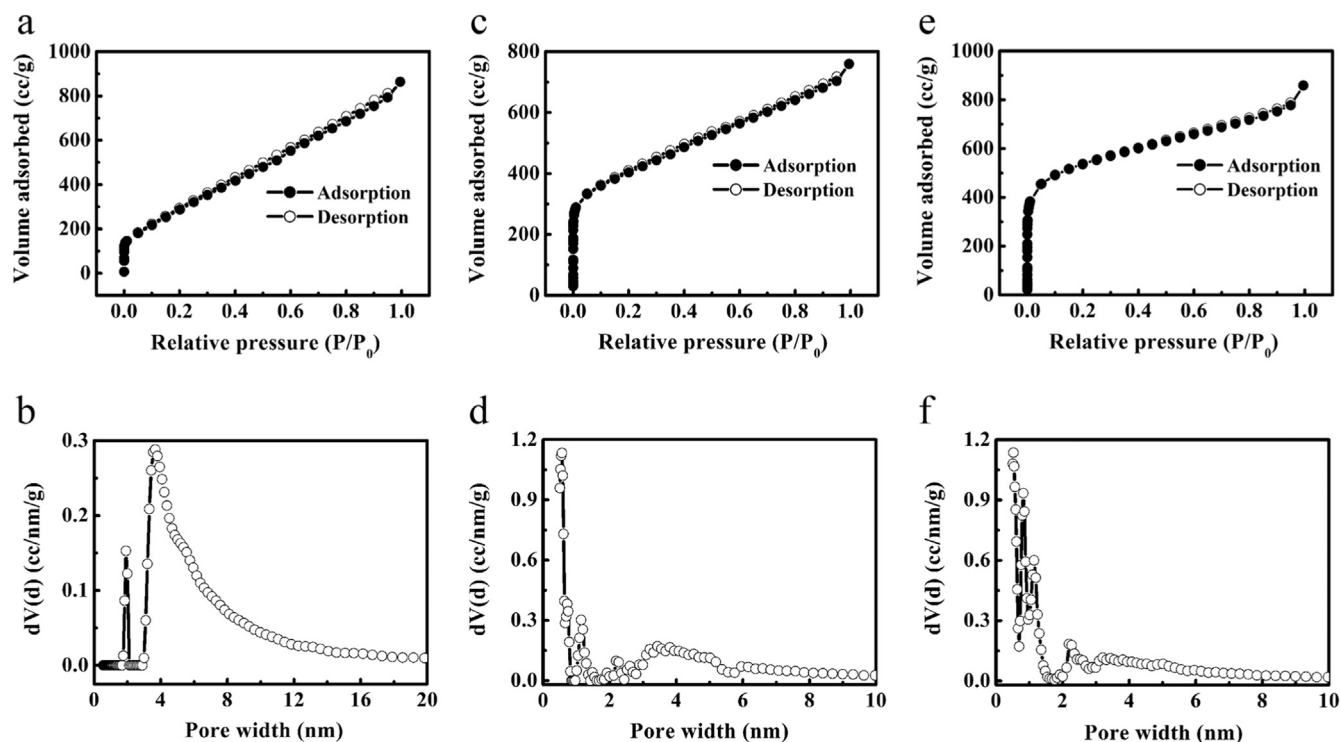
Fig. 3. Nitrogen adsorption-desorption isotherm and pore size distribution of (a–b) the Control, (c–d) the PCNS-4, and (e–f) the PCNS-6 samples.

Table 1
Pore structural parameters and compositions of the samples.

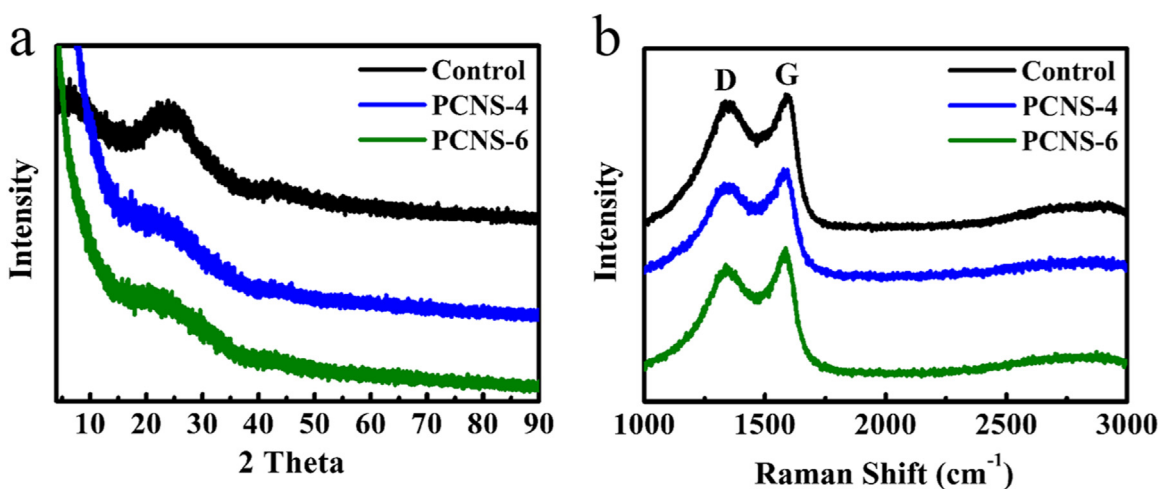| Sample	S_{BET} (m² g⁻¹)	S_{DFT} (m² g⁻¹)	V_{total} (cm³ g⁻¹)	V_{micro} (cm³ g⁻¹)	C (%)	O (%)	N (%)
Control	1055	1037	1.34	0.39	83.98	12.99	3.03
PCNS-4	1424	1669	1.18	0.59	93.97	5.21	0.82
PCNS-6	1947	1991	1.33	0.80	94.45	4.90	0.65

Fig. 4. (a) XRD patterns and (b) Raman spectra of the Control, PCNS-4 and PCNS-6 samples.

accessible surface area may play a more important role than the absolute value of SSA. This is fully consistent with our results, where the rather high capacitance (470 F g⁻¹) with a modest SSA (1947 m² g⁻¹) evidently indicates the high accessible surface area of the PCNS-6. Besides the high density of micropores which lead to a high capacity for ion storage, the high performance of PCNS-6 is owed to the 3-D scaffolding framework, which not only gains the high accessible surface area, but also shortens the ion diffusion pathway on a large

electrode/electrolyte interface and facilitates rapid ion transfer. In addition, the heteroatom doping also provides the Faradic contribution with EDLC.

3.3. Electrochemical properties in a two-electrode system using aqueous electrolyte

The capacitive behavior of the PCNS-6 sample using 6 mol L⁻¹
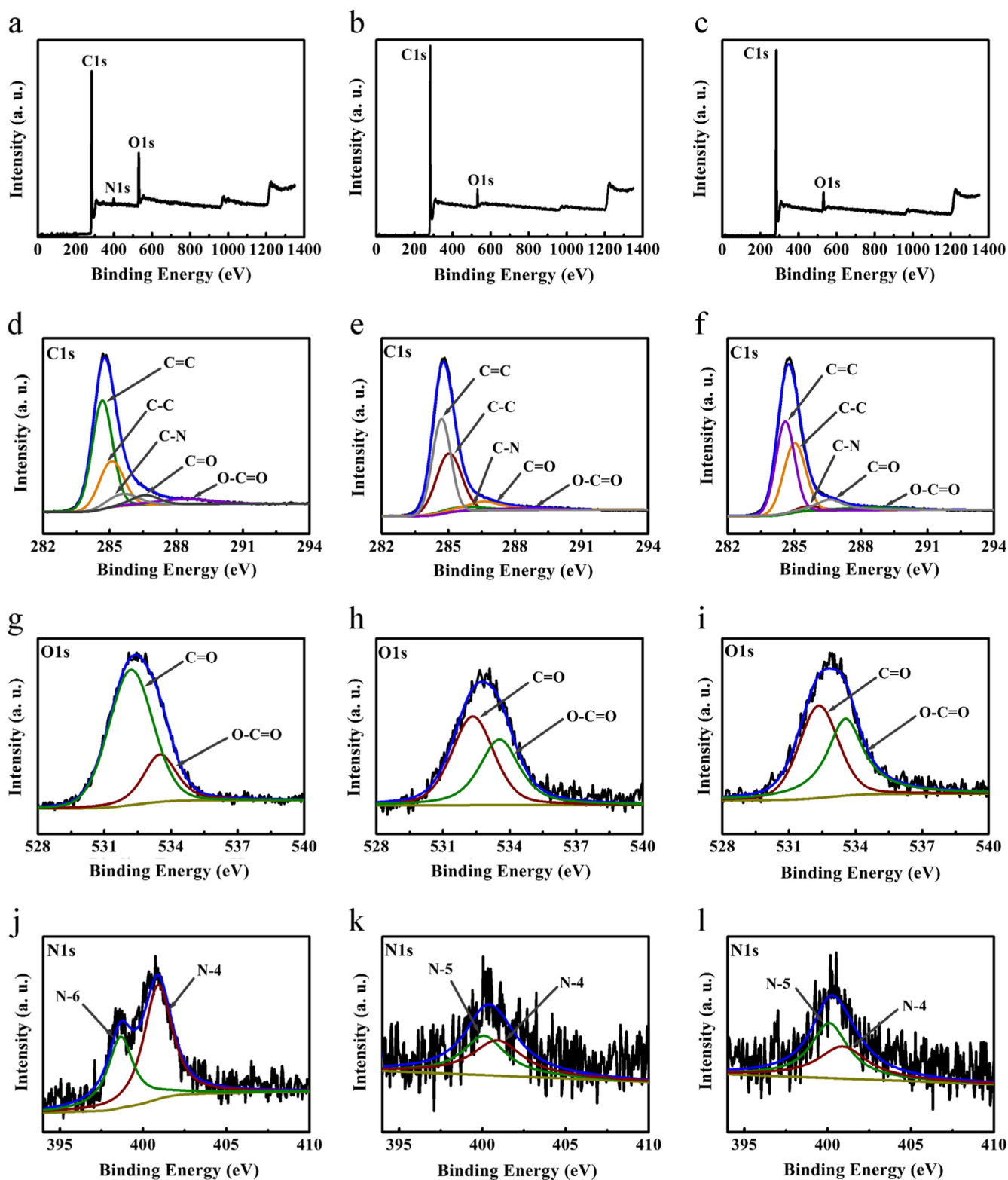
Fig. 5. XPS results of the Control, PCNS-4 and PCNS-6 samples. (a–c) XPS survey, (d–f) C1s spectra, (g–i) O1s spectra, and (j–l) N1s spectra. The left, middle and right columns are the results from the Control, PCNS-4 and PCNS samples, respectively.

KOH as the aqueous electrolyte was also investigated in a two-electrode system. The CV curve of the PNCS-6 (Fig. 7a) exhibited a good rectangular shape even at a rate as high as 200 mV s^{-1}. Especially, a specific capacitance as high as 72% of the highest value was obtained at 200 mV s^{-1} (Fig. 7b). And again, the quasi-linear galvanostatic charge-discharge curve at different current densities confirmed its good EDLC feature (Fig. 7c). The calculated specific capacitance of the PCNS-6 was 310 F g^{-1} at a current density of 1 A g^{-1}, much higher than that of the reported two-dimensional (2-D) PCNS (e.g. 228 F g^{-1} at a current density of 1 A g^{-1} [6]). Furthermore, a high capacitance retention was also achieved in this case, e.g. 64% even at 20 A g^{-1}.
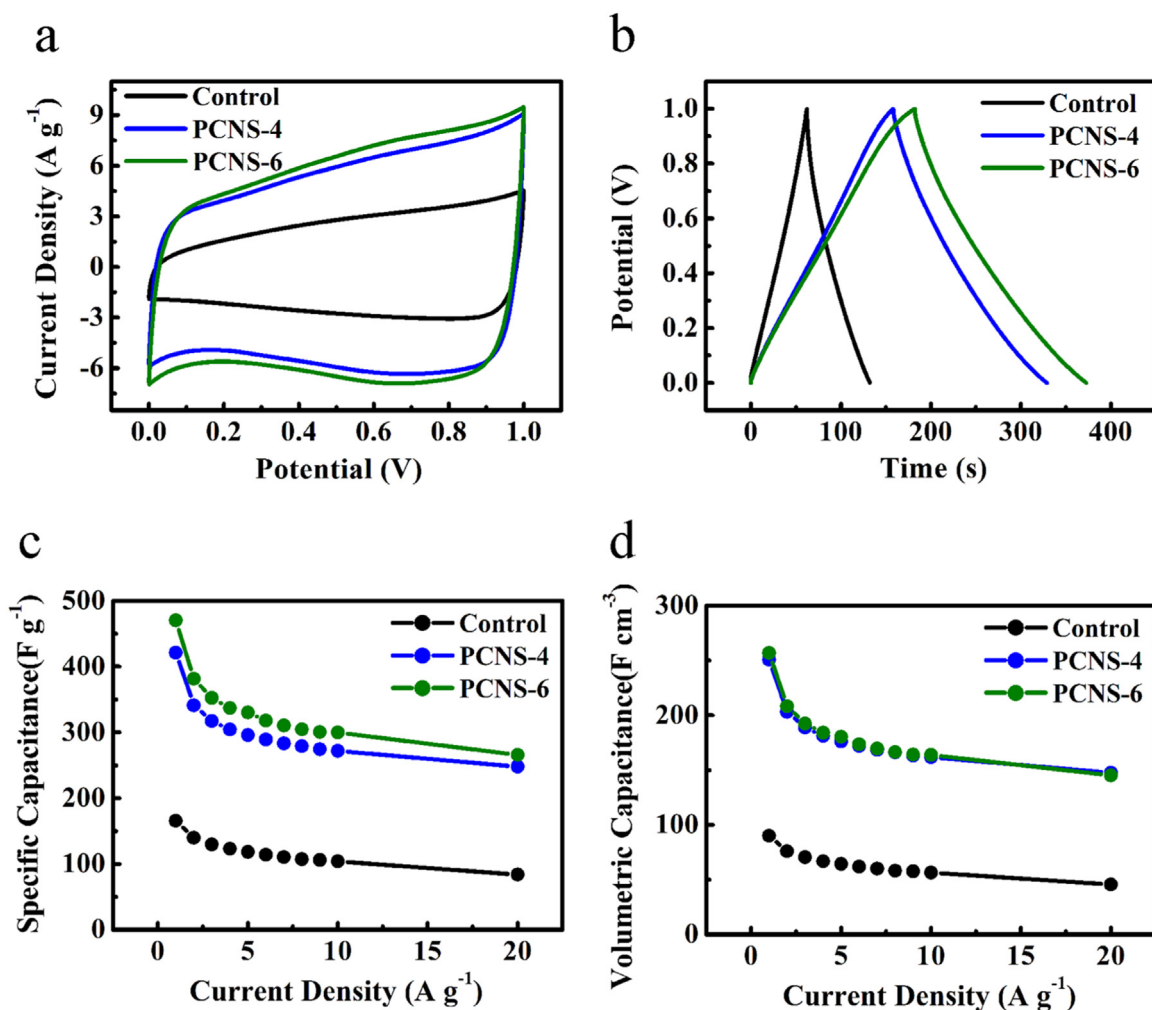
Fig. 6. Electrochemical performance of the Control, PCNS-4, PCNS-6 samples measured in a three-electrode system using 6 mol L^{-1} KOH as the electrolyte. (a) CV curves at 20 mV s^{-1}; (b) The galvanostatic charge-discharge profiles at 2 A g^{-1}; (c) Gravimetric capacitances at different current densities from 1 to 20 A g^{-1}. (d) Volumetric capacitances at different current densities.

Table 2
Specific capacitance of reported carbon-based supercapacitors.

Materials	Activating agent	BET surface area (m^2 g^{-1})	Test system[a]	Electrolyte	Current density	Specific capacitance (F g^{-1})	Ref. no.
Gelatin	KOH	2774	2E	6 M KOH	0.5 A g^{-1}	300	[6]
Silk	KOH	2557.3	2E	1 M H$_2$SO$_4$	0.1 A g^{-1}	264	[14]
Protein	N/A	805.7	3E	1 M H$_2$SO$_4$	0.2 A g^{-1}	390.4	[15]
Yogurt	KOH	1300	2E	6 M KOH	2 A g^{-1}	225	[18]
Eggshell membrane	Air	221.2	3E	1 M KOH	0.2 A g^{-1}	297	[19]
Human hair	KOH	1306	3E	6 M KOH	1 A g^{-1}	340	[20]
Willow catkin	KOH	1533	3E	6 M KOH	0.5 A g^{-1}	298	[31]
Cotton	KOH	1563	3E	6 M KOH	0.1 A g^{-1}	314	[32]
Sugar	N/A	1005	2E	1 M H$_2$SO$_4$	1 A g^{-1}	250	[33]
Fungus	KOH	1103	3E	6 M KOH	0.5 A g^{-1}	374	[34]
Pomelo mesocarps	CaCl$_2$	974.6	3E	2 M KOH	0.5 A g^{-1}	245	[35]
Seaweeds	N/A	746	3E	1 M H$_2$SO$_4$	0.2 A g^{-1}	264	[36]
Bamboo byproduct	KOH	1472	3E	6 M KOH	0.1 A g^{-1}	301	[37]
Shiitake mushroom	KOH	2988	3E	6 M KOH	1 A g^{-1}	306	[38]
DES in this work	KOH	1947	3E	6 M KOH	1 A g^{-1}	470	

[a] 2E/3E refers to a two-electrode/three-electrode system test.

As another critical factor to evaluate the potential for practical applications, the cyclic stability of the PCNS-6 electrode-based supercapacitors was examined using galvanostatic charge-discharge curves collected at a current density of 10 A g^{-1} (Fig. 7e). Excitingly, it was found that the capacitance retention was remarkably high, with more than 98% maintained after 50,000 charge-discharge cycles, indicating the excellent long-term cyclic stability. Fig. 7f shows the Nyquist plots of the PCNS-6 electrode-based supercapacitors in the frequency ranging from 10 kHz to 10 MHz. The vertical lines at a low frequency region confirm the dominance of EDLC as well as the good capacitive performance and the high cycle stability. The Nyquist plot expanded in the high
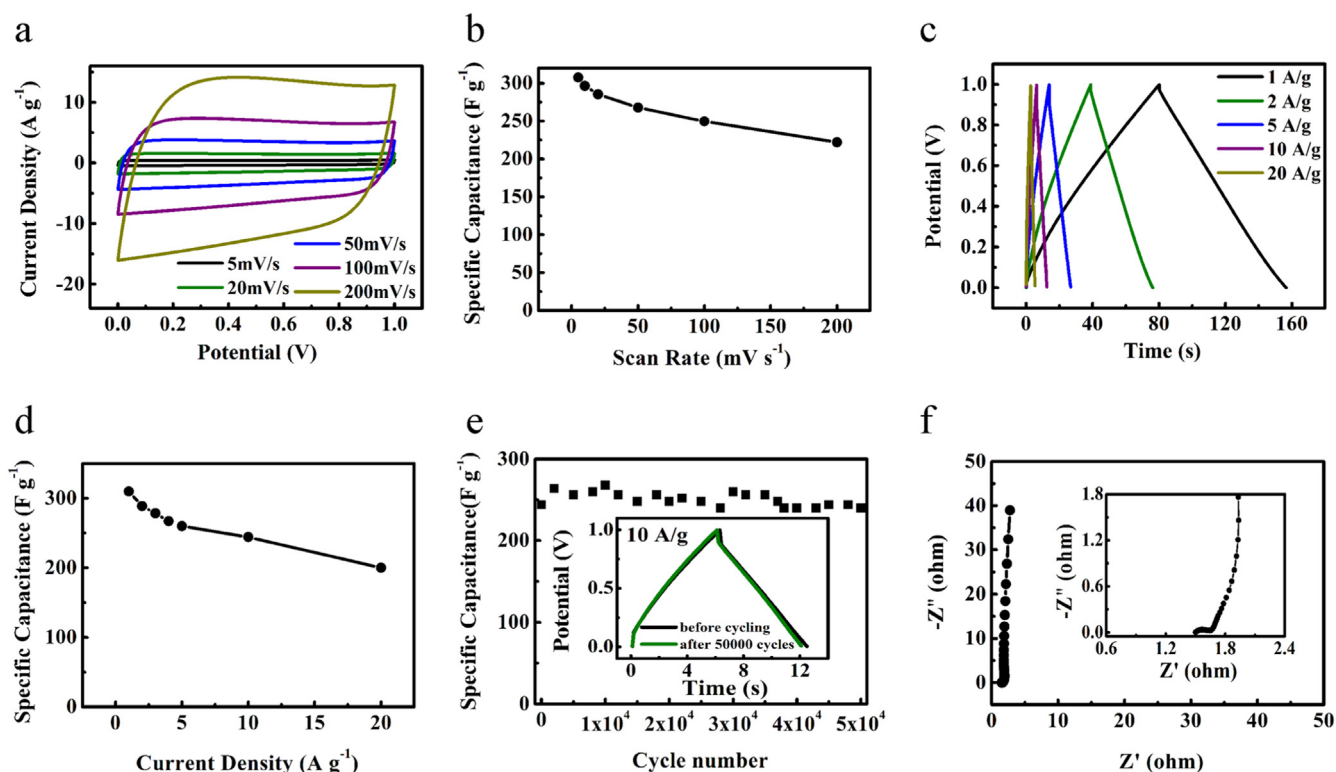
Fig. 7. Electrochemical performance characteristics of the PCNS-6 measured in a two-electrode system using 6 mol L^{-1} KOH as the electrolyte. (a) CV curves at different scan rates from 5 to 200 mV s^{-1} in a voltage window from −1.0 to 0 V. (b) Specific capacitance of the samples calculated from CV curves. (c) Charge-discharge curves at different current densities from 1 to 20 A g^{-1}. (d) Specific capacitance of the samples calculated from galvanostatic charge-discharge curves. (e) Cycling stability measured at 10 A g^{-1}. The inset: the magnified galvanostatic charge-discharge curves before and after 50,000 cycles. (f) Nyquist plots under the influence of an amplitude of 5 mV.

frequency region is presented in the inset. The short length of the Warburg-type lines (the 45° segment) indicates the low resistance of ion transportation and high ion diffusion efficiency. The equivalent series resistances obtained was 1.5 Ω, pointing out the good conductivity of our product.

3.4. Electrochemical properties in a two-electrode system using ionic liquids electrolyte

Electrochemical performance of the PCNS-6 in a two-electrode system using EMIMBF$_4$ as the ionic liquids was examined. Similar to the above studies, the rectangular CV curves at various scan rates (Fig. 8a) ranging from 5 to 200 mV s^{-1} confirmed the good rate of the PCNS-6 sample. And their nearly symmetric triangular shape in a current-density range of 0.25–10 A g^{-1} indicates its highly reversible charge-discharge behavior (Fig. 8b). The specific capacitance calculated from the charge-discharge measurements at different charging rates is shown in Fig. 8c. A specific capacitance as high as 173 F g^{-1} was achieved at 0.25 A g^{-1}, much higher than that of the reported 2-D PCNS (106 F g^{-1} at 1 A g^{-1} in 1 mol L^{-1} tetraethylammonium tetra-fluoroborate/acetonitrile electrolyte) [6] and interconnected carbon nanosheets (122F g^{-1} at 1 A g^{-1} in(1-butyl-1-methylpyrrolidinium bis-(trifluoromethylsulfony)imide electrolyte) [17]. Furthermore, high capacitance retention (47%) was achieved when the charging current was increased to as high as 40 folds. Fig. 8d displays the capacitance retention of the PCNS-6 electrode-based supercapacitors at a current density of 5 A g^{-1} upon 5000 cycles. The specific capacitance was decreased slightly and can be maintained about 87% of the initial value after 5000 cycles. These results are consistent with the Nyquist plots of the PCNS-6 electrode-based supercapacitors (frequency ranging from 10 kHz to 10 MHz with a signal amplitude of 5 mV, Fig. 8e). Shown by the high frequency region in the inset, the length of the Warburg-type lines, charge transfer resistance and equivalent series resistances (ESR) were

slightly increased after 5000 cycles.

Fig. 8f shows the Ragone plots of the PCNS-6, *i.e.* the energy density as a function of the power density, measured in the two-electrode cell supercapacitors, using the aqueous electrolyte and ionic liquids, respectively. It was found that the energy density can reach as high as 43.0 Wh kg^{-1} with a power density of 500 W kg^{-1} whereas the energy density decreased to 22.2 Wh kg^{-1} when the power density was increased to 20,000 W kg^{-1} in the aqueous electrolyte. The values are superior to those of cases reported previously, such as nitrogen and sulfur co-doped PCNS (21.0 Wh kg^{-1} at 180 W kg^{-1}) [31], gelatin-based microporous carbon nanosheets (7.43 Wh kg^{-1} at 263.5 W kg^{-1}) [39], nitrogen-doped interconnected carbon nanosheets (14.7 Wh kg^{-1} at 90 W kg^{-1}) [35] and carbon nanofibers-bridged PCNS (20.4 Wh kg^{-1} at 81.8 W kg^{-1}) [40]. More importantly, using ionic liquids, the PCNS-6 based supercapacitors can provide a high power density of 15 kW/kg at an energy density of 25.4 Wh kg^{-1} and a high energy density of 54.1 Wh kg^{-1} at a power density of 375 W kg^{-1} at room temperature. The values are significantly higher than those ever reported from PCNS-based supercapacitors using organic electrolyte [6,41,42]. Furthermore, we assembled a prototype supercapacitor device using the PCNS-6 as the electrode materials to light 15 LED bulbs aligned in an 'HIT' shape (where 'HIT' is the abbreviation of our university, Fig. 8g) and drive a small fan (Fig. 8e, the video is presented in the supporting online information) to directly demonstrate its excellent performance on energy storage.

Supplementary material related to this article can be found online at http://dx.doi.org/10.1016/j.nanoen.2016.07.020.

3.5. Universality for the formation of 3-D scaffolding PCNS framework

As mentioned above, we achieved AC frameworks with a high accessible SSA, high-density of micropores and heteroatom doping from
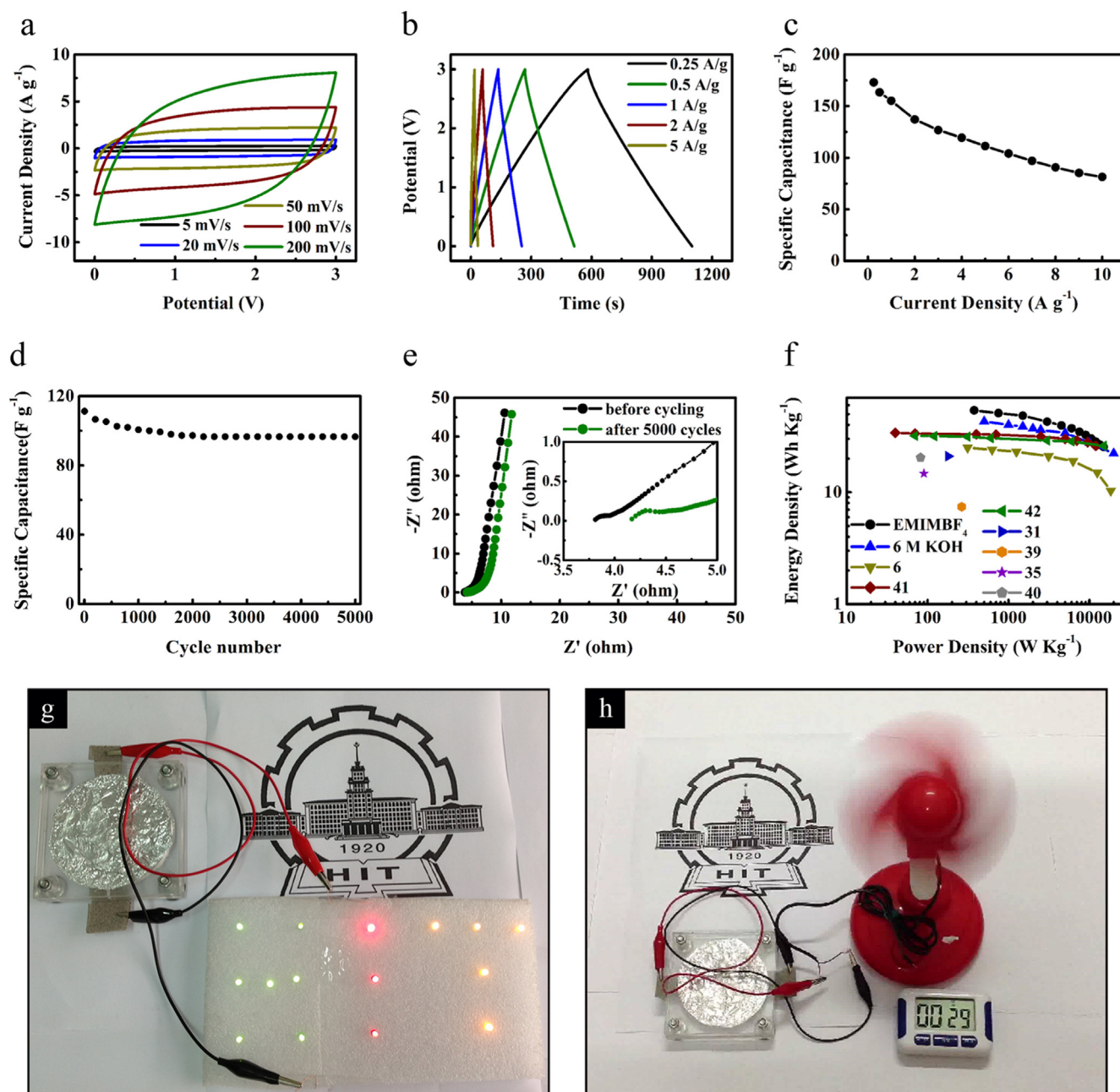
Fig. 8. Electrochemical performance characteristics of the PCNS-6 measured in a two-electrode system using EMIMBF$_4$ electrolyte. (a) CV curves at different scan rates from 5 to 200 mV s^{-1} in a voltage window from 0 to 3 V. (b) Charge-discharge curves at different current densities from 0.25 to 5 A g^{-1}. (c) Gravimetric capacitances at different current densities. (d) Cycling stability measured at 5 A g^{-1}. (e) Nyquist plots before and after 5000 cycles. (f) Ragone plot of the PCNS-6, in comparison with reported results. Photographs of (g) 15 LEDs and (h) a small fan powered by the supercapacitor device.

DES, a typical plant waste, *via* a rather simple treatment, and verified the excellent performance for energy storage, with the capacitance, energy density, power density, capacitance retention, cycle stability among the highest ever reported. Even so, without an extended investigation, this is merely another individual case of utilizing biowastes to produce high-performance ACs. It would be far more important to unravel the common features of promising plant-waste candidates for the 3-D scaffolding PCNS frameworks. We explored, therefore, a variety of different biomass, including willow catkin, poplar catkin, rose petals, seaweed, tremella, and so on, using the same carbonization and activation procedure for DES. It was revealed that none of them induced the 3-D framework. Although these obtained ACs showed good capacitive properties, they were significantly inferior to the DES frameworks. Very excitingly, over a great deal of attempts, we found that a series of

plant wastes sharing a common feature with DES, *i.e.* half transparent thin flakes, indeed leaded to the formation of the 3-D scaffolding PCNSs frameworks in all cases, as demonstrated by the examples in Fig. 9, *i.e.* the dry skin of onion and garlic. The capacitive properties of PCNS samples derived from them were investigated respectively in a three- and two-electrode system using 6 mol L^{-1} KOH electrolyte (Figs. S4 and S5), revealing the promising performance in all cases. Not only the lamellar thin flakes can benefit a facile reaction with KOH, we speculate that the special subtle structure and composition of these natural materials may also contribute to the formation of the skeleton of the framework, given that all of them are plant epidermis rich in protein, carbohydrate and cellulose. Meanwhile, KOH can react with the carbon flakes following $6KOH + C \leftrightarrow 2K + 3H_2 + 2K_2CO_3$ to form monoclinic phase $K_2CO_3 \cdot 1.5H_2O$ (Fig. S3) which was removed by HCl later. The
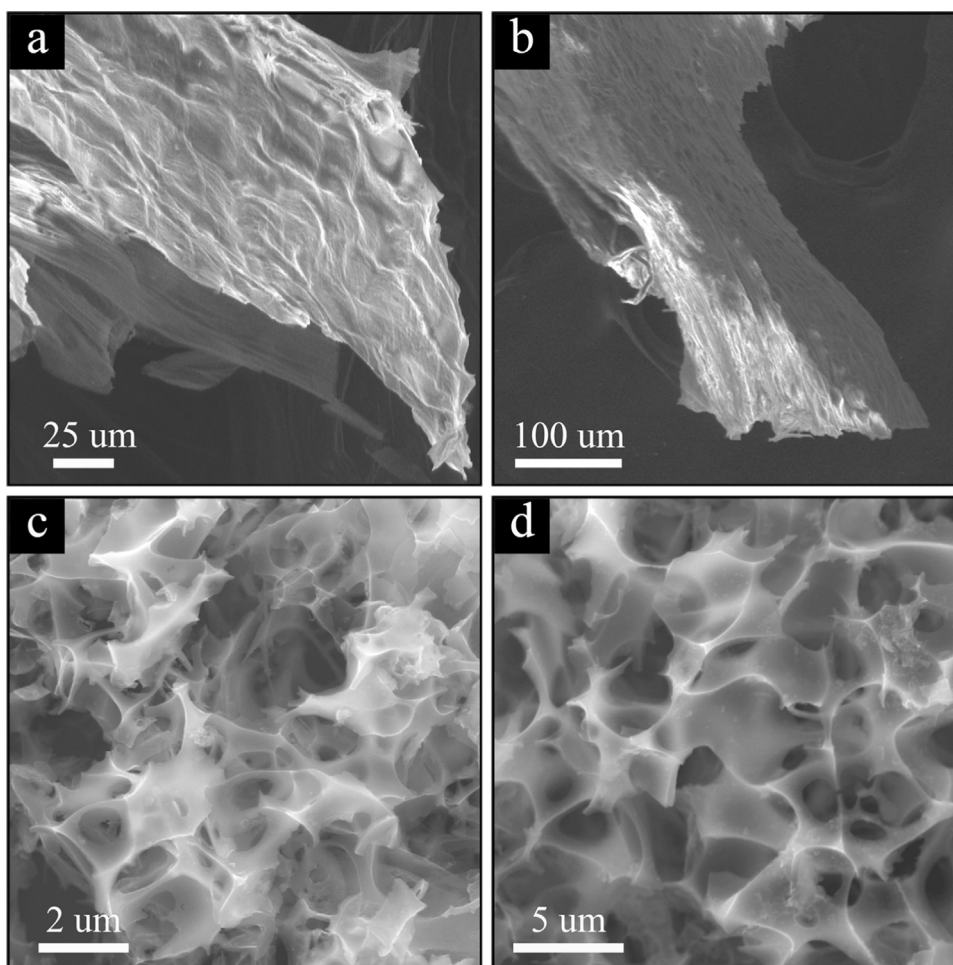
Fig. 9. SEM images of garlic skin and onion skin (a–b) after drying and (c–d) after carbonization plus KOH activation at a KOH concentration of 6 mol L^{-1}.

procedure is likely to reduce the thickness of the flakes to be nanosheets and generate plenty of microporosity simultaneously, as supported by the literature [14,17].

4. Conclusion

We report a facile and scalable synthesis of 3-D scaffolding PCNSs frameworks from plant wastes, using dry elm samara as the prototype. The products possess a high accessible SSA induced by the 3-D framework, a high density of micropores as well as heteroatom doping, enabling large ion storage and high-rate ion transfer, with both EDLC and faradic contribution. The PCNS-6 exhibited a rather high charge storage capacity with a specific capacitance of 470 F g^{-1} and 310 F g^{-1} at a current density of 1.0 A g^{-1} respectively in a three- and two-electrode system using 6 mol L^{-1} KOH electrolyte, among the highest ever reported for carbon materials derived from biomass. Meanwhile, the results also revealed a high rate capability (72% and 64% capacitance retention at 200 mV s^{-1} and 20 A g^{-1}, respectively) as well as a high cycling stability (2% loss over 50,000 cycles) together with an energy density as high as 22.2 Wh kg^{-1} at the power density of 20,000 W kg^{-1}. Most importantly, it is unraveled that such 3-D scaffolding PCNSs frameworks can be easily achieved from a series of different plant wastes sharing the common feature, i.e. half-transparent thin epidermis flakes. This work may have provided a clear strategy on how to select the right candidates from innumerable biomass for ACs on high-performance supercapacitors. Such 3-D porous carbon materials derived from low-cost, sustainable and abundant biowastes and produced by facile and large-scale production may have substantial potential for energy storage, gas sensing, air/water purification, catalysis, and biological applications.

Author contributions

C.C. and M. Y. designed the experiments; C. C., D. Y. and G. Z. performed experiments; C. C., D. Y., G. Z., B. D., W. T., L. S. characterized the samples and analyzed the data; C.C., M. Y., Y. S. and F. B. wrote the paper. All authors have approved the final version of the manuscript.

Appendix A. Supporting information

Supplementary data associated with this article can be found in the online version at http://dx.doi.org/10.1016/j.nanoen.2016.07.020.

References

[1] M. Sevilla, R. Mokaya, Energy Environ. Sci. 7 (2014) 1250–1280.
[2] P. Simon, Y. Gogotsi, Nat. Mater. 7 (2008) 845–854.
[3] L. Qie, W.M. Chen, H.H. Xu, X.Q. Xiong, Y. Jiang, F. Zou, X.L. Hu, Y. Xin, Z. L. Zhang, Y.H. Huang, Energy Environ. Sci. 6 (2013) 2497–2504.
[4] J.L. Huang, J.Y. Wang, C.W. Wang, H.N. Zhang, C.X. Lu, J.Z. Wang, Chem. Mater. 27 (2015) 2107–2113.
[5] X.Y. Zheng, J.Y. Luo, W. Lv, D.W. Wang, Q.H. Yang, Adv. Mater. 27 (2015) 5388–5395.
[6] X.M. Fan, C. Yu, J. Yang, Z. Ling, C. Hu, M.D. Zhang, J.S. Qiu, Adv. Energy Mater. 5 (2014) 1401761–1401767.
[7] Y.W. Zhu, S. Murali, M.D. Stoller, K.J. Ganesh, W.W. Cai, P.J. Ferreira, A. Pirkle, R. M. Wallace, K.A. Cychosz, M. Thommes, D. Su, E.A. Stach, R.S. Ruoff, Science 332 (2011) 1537–1541.
[8] J.H. Hou, C.B. Cao, F. Idrees, X.L. Ma, ACS Nano 9 (2015) 2556–2564.
[9] P. Hao, Z.H. Zhao, J. Tian, H.D. Li, Y.H. Sang, G.W. Yu, H.Q. Cai, H. Liu, C.P. Wong, A. Umar, Nanoscale 6 (2014) 12120–12129.
[10] S.S. Zheng, H. Ju, X. Lu, Adv. Energy Mater. 5 (2015) 1500871–1500879.
[11] M.M. Titirici, R.J. White, N. Brun, V.L. Budarin, D.S. Su, F.D. Monte, J.H. Clarkd, M.J. MacLachlang, Chem. Soc. Rev. 44 (2015) 250–290.
[12] M.A. Yahya, Z. Al Qodah, C.W.Z. Ngah, Renew. New. Sustain. Energy Rev. 46 (2015) 218–235.
[13] L. Zhang, F. Zhang, X. Yang, K. Leng, Y. Huang, Y.S. Chen, Small 9 (2013) 1342–1347.
[14] Y.S. Yun, S.Y. Cho, J.Y. Shim, B.H. Kim, S.J. Chang, S.J. Baek, Y.S. Huh, Y. Tak, Y. W. Park, S. Park, H.J. Jin, Adv. Mater. 25 (2013) 1993–1998.
[15] Z. Li, Z.W. Xu, X.H. Tan, H.L. Wang, C.M.B. Holt, T. Stephenson, B.C. Olsen, D. Mitlin, Energy Environ. Sci. 6 (2013) 871–878.
[16] C.L. Long, L.L. Jiang, X.L. Wu, Y.T. Jiang, D.R. Yang, C.K. Wang, T. Wei, Z.J. Fan, Carbon 93 (2015) 412–420.
[17] H.L. Wang, Z.W. Xu, A. Kohandehghan, Z. Li, K. Cui, X.H. Tan, T.J. Stephenson, C. K. Kingondu, C.M.B. Holt, B.C. Olsen, J.K. Tak, D. Harfield, A.O. Anyia, D. Mitlin, ACS Nano 7 (2013) 5131–5141.
[18] M. Wahid, G. Parte, D. Phase, S. Ogale, J. Mater. Chem. A 3 (2015) 1208–1215.
[19] Z. Li, L. Zhang, B.S. Amirkhiz, X.H. Tan, Z.W. Xu, H.L. Wang, B.C. Olsen, C.M. B. Holt, D. Mitlin, Adv. Energy Mater. 2 (2012) 431–437.
[20] W.J. Qian, F.X. Sun, Y.H. Xu, L.H. Qiu, C.H. Liu, S.D. Wang, F. Yan, Energy Environ. Sci. 7 (2014) 379–386.
[21] D.P. Osborne, Bird Study 30 (1983) 27–38.
[22] G.P. Hao, A.H. Lu, W. Dong, Z.Y. Jin, X.Q. Zhang, J.T. Zhang, W.C. Li, Adv. Energy Mater. 3 (2013) 1421–1427.
[23] M.A. Pimenta, G. Dresselhaus, M.S. Dresselhaus, L.G. Cancado, A. Jorio, R. Saito, Phys. Chem. Chem. Phys. 9 (2007) 1276–1291.
[24] G.X. Li, Y.L. Li, X.M. Qian, H.B. Liu, H.W. Lin, N. Chen, Y.J. Li, J. Phys. Chem. C 115 (2011) 2611–2615.
[25] G.X. Li, Y.L. Li, H.B. Liu, Y.B. Guo, Y.J. Li, D.B. Zhu, Chem. Commun. 46 (2010) 3256–3258.
[26] J.S. Zhou, J. Lian, L. Hou, J.C. Zhang, H.Y. Gou, M.R. Xia, Y.F. Zhao, T.A. Strobel, L. Tao, F.M. Gao, Nat. Commun. 6 (2015) 8503–8511.
[27] J.L. Figueiredo, M.F.R. Pereira, Catal. Today 150 (2010) 2–7.
[28] D. Usachov, O. Vilkov, A. Grüneis, D. Haberer, A. Fedorov, V.K. Adamchuk, A. B. Preobrajenski, P. Dudin, A. Barinov, M. Oehzelt, C. Laubschat, D.V. Vyalikh, Nano Lett. 11 (2011) 5401–5407.
[29] L. Hao, X.L. Li, L.J. Zhi, Adv. Mater. 25 (2013) 3899–3904.
[30] D.W. Wang, F. Li, M. Liu, G.Q. Lu, H.M. Cheng, Angew. Chem. Int. Ed. 47 (2008) 373–376.
[31] Y.J. Li, G.L. Wang, T. Wei, Z.J. Fan, P. Yan, Nano Energy 19 (2016) 165–175.
[32] K. Song, W.L. Song, L.Z. Fan, J. Mater. Chem. A 3 (2015) 16104–16111.
[33] X.B. Wang, Y.J. Zhang, C.Y. Zhi, X. Wang, D.M. Tang, Y.B. Xu, Q.H. Weng, X. F. Jiang, M. Mitome, D. Golberg, Y. Bando, Nat. Commun. 4 (2013) 2905–2913.
[34] C.L. Long, X. Chen, L.L. Jiang, L.J. Zhi, Z.J. Fan, Nano Energy 12 (2015) 141–151.
[35] H. Peng, G.F. Ma, K.J. Sun, Z.G. Zhang, Q. Yang, Z.Q. Lei, Electrochim. Acta 190 (2016) 862–871.
[36] E.R. Piñero, M. Cadek, F. Béguin, Adv. Funct. Mater. 19 (2009) 1032–1039.
[37] W.Q. Tian, Q.M. Gao, Y.L. Tan, K. Yang, L.H. Zhu, C.X. Yang, H. Zhang, J. Mater. Chem. A 3 (2015) 5656–5664.
[38] P. Cheng, S.Y. Gao, P.Y. Zang, X.F. Yang, Y.L. Bai, H. Xu, Z.H. Liu, Z.B. Lei, Carbon 93 (2015) 315–324.
[39] H.L. Fan, W.Z. Shen, ACS Sustain. Chem. Eng. 4 (2016) 1328–1337.
[40] Y.T. Jiang, J. Yan, X.L. Wu, D.D. Shan, Q.H. Zhou, L.L. Jiang, D.R. Yang, Z.J. Fan, J. Power Sources 307 (2016) 190–198.
[41] M. Sevilla, A.B. Fuertes, ACS Nano 8 (2014) 5069–5078.
[42] A.B. Fuertes, M. Sevilla, ACS Appl. Mater. Interfaces 7 (2015) 4344–4353.

Chong Chen received his B.E. and M.S. degree from Hefei University of Technology, China. He is now a PhD candidate at School of Chemistry and Chemical Engineering in Prof. Miao Yu's group at Harbin Institute of Technology, China. His research interests focus on the fabrication of functional nanomaterials and their applications in energy storage, catalysis and sensing.

Dengfeng Yu received his B.E. degree from Harbin Institute of Technology in 2014 and now is a postgraduate in Professor Ye Sun's group at School of Science, Harbin Institute of Technology, China. His current research interests focus on the carbon materials derived from biomass and their applications in high-performance supercapacitors and chemical sensors.

Gongyuan Zhao received his B.E. and M.S. degree from Northeast Forestry University in 2012 and 2015 respectively. He is now a PhD candidate in School of Chemistry and Chemical Engineering at Harbin Institute of Technology, China, with Prof. Miao Yu as his supervisor. His current research interests focus on the synthesis of carbon materials, such as carbon nanotubes, graphene, activated carbons and their applications in energy storage.

BaoSheng Du received his B.E. in 2011 from Suihua University and is now pursuing his PhD degree in Prof. Ye Sun's group at Harbin Institute of Technology, China. His current research interests cover the synthesis and processing of carbon nanomaterials and metal oxides together with their applications in photoluminescence and electrochemical energy storage.

Wei Tang received his B.E. degree from Harbin University in 2009 and now is a PhD candidate in Condensed Matter Science and Technology Institute at Harbin Institute of Technology, supervised by Prof. Ye Sun. His current research interests focus on rare earth doped oxide nanomaterials and their applications in temperature-sensing devices and gas-sensing devices.

Lei Sun received his B.E. and M.S. degree from Changchun University of Technology in 2008 and 2012, respectively. He is pursuing his PhD degree at School of Chemistry and Chemical Engineering, Harbin Institute of Technology, China. His research interests focus on the synthesis and modification of nanostructured metal oxides and their applications in photocatalysis and antitumor photothermal therapy.

Flemming Besenbacher received his PhD degree from Aarhus University (AU), Denmark. He is a full professor at the Department of Physics of AU since 1996 and was the Director of the Interdisciplinary Nanoscience Center (iNANO) from 2002 to 2012. His research interests cover scanning tunneling microscopy, atomic force microscopy, fabrication and function of nanoclusters, hydrogen storage, photocatalytic nanomaterials, and sustainable energy materials.

Ye Sun received his PhD degree in chemistry from University of Bristol (UK) in 2007, and then worked at Cardiff University (UK) and Aarhus University (Denmark) as a postdoctoral fellow from 2007 to 2011. Since 2011, he is a full professor at School of Science, Harbin Institute of Technology, China. His research interests cover photoluminescence, photocatalysis, high-performance carbon materials for energy storage, temperature/gas sensing, biosensors, bioimaging, and multi-modal antitumor therapies.

Miao Yu received her PhD degree from Warwick University in 2007, and then worked at Aarhus University, Harvard University and Massachusetts Institute of Technology as a postdoctoral fellow. Since 2011, she is a full professor at School of Chemistry and Chemical Engineering, Harbin Institute of Technology, China. Her research interests cover energy storage, *in situ* reaction on surfaces, multifunctional antitumor nanoagents, bioimaging, and photocatalytic nanomaterials.